Available online at www.sciencedirect.com
ScienceDirect
Polymer 48 (2007) 6404–6414
polymer
www.elsevier.com/locate/polymer

Thermal and structural properties of blends of isotactic with atactic polystyrene

Huipeng Chen, Hui Xu, Peggy Cebe*

Department of Physics and Astronomy, Tufts University, STC-208, 4 Colby Street, Medford, MA 02155, USA

Received 4 May 2007; received in revised form 24 July 2007; accepted 2 August 2007
Available online 8 August 2007

Abstract

Blends of isotactic polystyrene (iPS) with non-crystallizable atactic polystyrene (aPS) were studied by differential scanning calorimetry and small angle X-ray scattering. The iPS/aPS blends, prepared by solution casting, were found to be miscible in the melt over the entire composition range. Both quenched amorphous and semicrystalline blends exhibit a single, composition-dependent glass transition temperature, depressed from that of either of the homopolymer components. Addition of aPS causes a decrease in crystallinity and in the rigid amorphous fraction, and suppression of the reorganization/recrystallization of iPS during thermal scanning: only one melting peak is observed for blends with larger aPS content. Formation and devitrification of the rigid amorphous fraction of iPS are also affected by aPS addition. The annealing peak, which is due to the relaxation of rigid amorphous fraction in parallel with melting of a tiny amount of crystals, is retarded with an increase of the composition of aPS, resulting in the slow devitrification of RAF in parallel with the melting of large amount of crystals. X-ray scattering shows that the long period in the iPS/aPS blends is greater than in the iPS homopolymer, and long period increases slightly as aPS content increases. Comparison of the volume fraction of phase 1 with the volume fraction crystallinity from DSC suggests that more and more amorphous phase is rejected outside the lamellar stacks as aPS content increases. The effect of aPS addition is to reduce the confinement of the amorphous phase chains. The cooperativity length, ξ_A, which is calculated from thermal analysis of the T_g region, increases with aPS addition. The interlamellar and extra-lamellar amorphous chains both contribute to the glass transition relaxation process.

Keywords: Isotactic polystyrene; iPS/aPS blends; Rigid amorphous fraction

1. Introduction

Polystyrene (PS) is a widely used engineering thermoplastic with good thermal stability. Three steric isomers of polystyrene include the crystallizable isotactic (iPS) and syndiotactic (sPS) forms, and non-crystallizable atactic (aPS) variant. The thermal and structural properties of binary blends of sPS with either iPS or aPS have been reported [1–3]. However, little work has been performed on binary blends of iPS and aPS, in which only the iPS component can crystallize [4–9]. The phase structure controls many of the physical properties of polymer blends, and we are particularly interested in studying the impact of the systematic addition of a non-crystallizable component on the structure. Our group has investigated several important binary blends of this type including poly(vinylidene fluoride) (PVF_2)/poly(methyl methacrylate) (PMMA) and poly(butylene terephthalate) (PBT)/polyarylate (PAr), both of which have been extensively studied [10–13]. In the present work, we investigate iPS/aPS blends, which are miscible in the quenched amorphous state. Upon crystallization of the iPS component, phase separation occurs. We utilize thermal analysis and X-ray scattering methods to study the crystalline and amorphous fractions, and the lamellar organization of crystalline iPS/aPS blends over the entire composition range.

Many semicrystalline polymers cannot be described using a conventional two-phase model comprising crystalline fraction and amorphous fraction. A three-phase model, comprising crystalline fraction (C), mobile amorphous fraction (MAF),

* Corresponding author. Tel.: +1 617 627 3365; fax: +1 617 627 3744.
E-mail address: peggy.cebe@tufts.edu (P. Cebe).

0032-3861/$ - see front matter © 2007 Elsevier Ltd. All rights reserved.
doi:10.1016/j.polymer.2007.08.006

and rigid amorphous fraction (RAF), has been applied in the study of well-crystallized bulk film of isotactic polystyrene, iPS [14–17]. Like other semicrystalline polymers such as poly(ethylene terephthalate), PET [18], poly(etheretherketone), PEEK [19], poly(phenylene sulfide), PPS [20], the RAF in iPS contributes neither to the heat of fusion of the crystals nor to the heat capacity change at the glass transition of the mobile amorphous phase. Layers of RAF were very thin (normally 2–4 nm) compared with that of MAF (normally 10–200 nm) and often suggested to be associated with the lamella crystals as an interfacial layer. The rigid amorphous fraction in blends has not yet been investigated widely. The formation and/or relaxation, and location, of RAF in blends of crystalline with non-crystalline polymers is still uninvestigated. An interesting question arises whether the addition of the non-crystalline blend partner, aPS, will affect the formation and/or devitrification of RAF.

There has been no literature yet reported on the melting behavior of iPS/aPS blends. For well-crystallized iPS homopolymer, either melt- or cold-crystallized, the RAF is established at the crystallization temperature, in parallel with the formation of crystals [14–17]. Three endothermic peaks are observed for the cold-crystallized iPS [14,15]. The lowest temperature peak is called the annealing peak. The other two endotherms, occurring at higher temperature, were assigned to the melting of crystals. Multiple melting peaks, with temperatures higher than the annealing peak, have been observed for both melt- and cold-crystallized iPS [14–17]. Several models have been proposed to explain this occurrence. One model is a melting–recrystallization–remelting model, in which the lower endotherm is due to the melting of original crystals and the higher one is due to the melting of crystals that recrystallized during heating after melting of the original crystals [21–25]. Another model is the dual-lamellar stack model, in which the multiple melting peaks are due to melting of two coexisting lamellar populations with different perfections [14–16,26,27]. Liu and Petermann, using transmission electron microscopy during heating, suggested this mechanism for iPS homopolymer [26]. At the annealing peak, no iPS crystals melted. IPS lamellae became ''broken'' at the lower of the two major melting endotherms, T_{m1}. The broken lamellae became repaired between T_{m1} and T_{m2}, which appeared as an exothermic peak in the DSC scan. Finally, the remaining parts of the lamellae melted at the uppermost endotherm, T_{m2}. Liu and Petermann suggested that crystal perfection varied within a single lamella because of tacticity variations [26], a result suggested by their earlier work [28], but they did not rule contributions from melting of a re-crystallized population during heating [26]. Our thermal study of iPS [14] supported the results of Liu and Petermann, and we suggested that the annealing peak was due to the devitrification of the RAF, possibly occurring in parallel with melting of some of crystals. An interesting question is whether the presence of aPS will affect the melting behavior of iPS lamellar crystals.

In the present work, binary blends of iPS with aPS were studied after melt-crystallization. We investigate the thermal properties and formation and devitrification of RAF for the iPS/aPS blends by differential scanning calorimetry (DSC). APS did impact the development of crystals and RAF, and inhibits the observation of the highest melting endotherm. Using small angle X-ray scattering (SAXS) combined with calorimetry, we investigated the lamellar structure for iPS/aPS blends.

2. Experimental section

2.1. Materials

Isotactic (90%) polystyrene powder with a weight average molecular weight of 400,000 g/mol and atactic polystyrene beads with a weight average molecular weight of 45,000 g/mol and density of 1.06 g/cm^3 were purchased from Scientific Polymer Products, Inc. iPS and aPS were dissolved separately in cyclohexanone with gentle heating to form stock solutions with concentrations of about 2% by weight of polymer. iPS/aPS blends were prepared by mixing the stock solutions to achieve the following weight ratios of iPS to aPS: 100/0, 90/10, 75/25, 65/35, 50/50, 40/60, 30/70, 10/90, and 0/100. Films of the blends were cast from solution, dried in a vacuum oven for several days, and then further dried at 210 °C for 30 min before being used in thermal measurements. The blends were heated to 250 °C for 2 min to eliminate crystal nuclei and then cooled at 20 °C/min and melt-crystallized at 190 °C for 12 h in a Mettler FP90 hot stage.

2.2. DSC measurements

DSC studies were carried out using TA Instruments temperature modulated DSC (TA Q100 and TA 2920 MDSC). Indium was employed for the temperature and heat flow calibration. The heat capacity was evaluated with respect to sapphire standard. Dry nitrogen gas was purged into the DSC cell with a flow rate of 50 mL/min. DSC measurements were performed at heating rates of 2 °C/min and 10 °C/min. Three runs were performed to obtain the heat capacity of all samples [14,29]. The first run is empty Al sample pan vs. empty Al reference pan to obtain baseline correction. The second run is sapphire standard vs. empty Al reference pan to calibrate heat flow amplitude. The third run is sample vs. the empty reference pan. All the empty Al reference pans and sample pans were kept at the same weight. The sample mass was kept at about 5–6 mg. Endotherms are presented with downward deflection in our scans.

Crystallinity was determined from the area of the DSC endotherm using 86.59 J/g as the heat of fusion of 100% crystalline iPS [30]. To compare crystallinity obtained with different methods, DSC mass fraction crystallinity, χ_c, was converted to volume fraction crystallinity, ϕ_c, using the amorphous and crystalline densities of iPS ($\rho_a = 1.06$ g/cc and $\rho_c = 1.11$ g/cc, respectively [30]):

$$\phi_c = (\chi_c \rho_a)/(\rho_c - \chi_c(\rho_c - \rho_a)). \quad (1)$$

2.3. X-ray scattering measurements

Wide and small angle X-ray scattering (WAXS, SAXS) intensity data were collected in transmission mode at Brookhaven National Laboratory, National Synchrotron Light Source at the X27C beam line. Two one-dimensional, gas filled wire detectors were used for WAXS and SAXS data collection. The wavelength (λ) was 0.1371 nm and the scattering vector, q ($q = 4\pi \sin\theta/\lambda$, for θ the half-scattering angle), was calibrated using silver behenate for SAXS, and silicon and sodelite for WAXS. Scattering patterns were recorded for 300 s at room temperature. The raw intensity data were corrected for detector linearity, sample absorption, background scattering, and changes in incident beam intensity. The Bragg long period (L_B) was determined from the position of the peak in the Lorentz-corrected SAXS intensity, $I(q)q^2$ vs. q.

After preliminary corrections, the final intensity, $I_{corr}(q)$, used for the calculation of the correlation function is determined. Behind the beam stop, the intensity is extrapolated from its value at the pixel location of the beam stop linearly to zero at $q = 0$. At high scattering vector, $I_{corr}(q \to \infty)$ is corrected to account for deviations from Porod's law behavior and thermal density fluctuations. The intensity at high q can be written as [31]:

$$I^{obs}(q \to \infty) = I^{ideal}(q)H^2(q) + I_{FL} \tag{2}$$

where $I^{ideal} = K_p/q^4$ (K_p is Porod's law constant); I_{FL} is a background due to short range fluctuations in the sample density [31]; and $H^2(q)$ is the Fourier transformation of the autocorrelation of the smoothing function, describing the deviations from Porod's law behavior caused by finite interphase thickness [32]. We assume a sigmoidal shape for the interphase geometry so that the form of H^2 is [32]:

$$H^2(q) = \exp\left(E^2q^2\right) \tag{3}$$

where the parameter, E, is a measure of the width of the interphase. At high q-vector, the intensity data are fitted with three adjustable parameters (K_p, I_{FL}, E).

The normalized one-dimensional electron density correlation function, $K(z)$, is evaluated along the direction, z, normal to the lamellar stacks from [33]:

$$K(z) = \int_0^\infty q^2 I_{corr}(q)\cos(qz)\mathrm{d}q \Big/ \int_0^\infty q^2 I_{corr}(q)\mathrm{d}q \tag{4}$$

The parameters: long period, L^{MAX}; thickness of phase 1, d_1; and V_1, the volume fraction of phase 1 within the lamellar stacks from the self-correlation triangle, are determined according to the method of Strobl and Schneider [34].

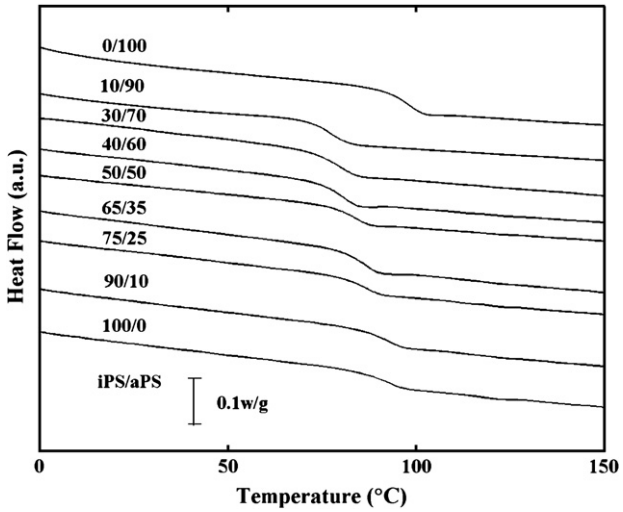

Fig. 1. DSC thermograms showing the glass transition region of iPS/aPS blends with the indicated compositions, melt-crystallized at 190 °C for 12 h and heated at 10 °C/min. Ordinate values have been normalized for total sample mass. The curves have been displaced vertically for clarity.

3. Results and discussion

3.1. Thermal analysis of the glass transition region

Fig. 1 shows the DSC thermograms for iPS/aPS blends in the vicinity of the glass transition after crystallization at 190 °C for 12 h. All the iPS/aPS blends exhibit a single glass transition temperature (T_g) and the T_gs of the blends lie at temperature below those of the pure components. The appearance of a single, composition-dependent T_g for the iPS/aPS blends indicates that the blends exhibit a homogeneous amorphous phase structure and that iPS is completely miscible with aPS over the entire composition range. Glass transition temperatures are summarized in Table 1.

Several relationships have been proposed to describe the dependence of T_g on the composition of miscible polymer blends [35–40]. Here we use Tsutsui's equation [37–39] to describe the T_g–composition relationship:

$$T_g = \left(W_1T_{g1} + W_2T_{g2}\right)/(W_1 + kW_2) + pW_1W_2/(W_1 + kW_2) \tag{5}$$

where T_g is the glass transition temperature of the blends; T_{g1} and T_{g2} are those of pure components (1 for iPS, 2 for aPS); W_1 and W_2 are the weight percents of iPS and aPS, respectively; k is an adjustable fitting parameter which can be taken as a quantity characterizing the strength of intermolecular interactions. The first term on the right-hand side of Eq. (5) is the Gordon–Taylor equation [36]. The second term represents intermolecular specific interactions in the mixture, accounting for effects of the rearrangements in the neighborhood of the molecular contacts. Some self-association interactions are broken and some inter-association interactions are formed [38,41]. Also there are some different forms for the second term. For example, Kwei [38] used (pW_1W_2) for the second

Table 1
Thermal properties of iPS/aPS semicrystalline blends[a]: glass transition temperature and heat capacity increment, crystal (C), mobile amorphous (M) and rigid amorphous (R) fractions

iPS/aPS	T_g (°C), ±0.2	ΔC_p (J/g K), ±0.001	χ_C[b], ±0.01[e]	χ_C[c], ±0.001[e]	χ_M[f], ±0.002	χ_R[d], ±0.003	χ_R/χ_C, ±0.05
100/0	94.0	0.183	0.36 ± 0.02	0.37 ± 0.01	0.541	0.093	0.25
90/10	93.1	0.192	0.338	0.34 ± 0.01	0.569	0.089	0.26
75/25	89.7	0.208	0.309	0.313	0.615	0.072	0.23
65/35	87.6	0.222	0.276	0.278	0.655	0.067	0.24
50/50	85.6	0.248	0.204	0.208	0.733	0.059	0.28
40/60	83.6	0.282	0.110	0.106	0.833	0.061	0.57
30/70	81.9	0.308	0.045	0.042	0.911	0.047	1.2
10/90	79.8	0.313	0.020	0.019	0.926	0.045	2.4
0/100	98.3	0.339	0	0	1	0	–

[a] Crystallized isothermally at 190 °C for 12 h.
[b] Obtained from heat of fusion, using Eq. (7).
[c] Obtained from heat capacity, using Eq. (10).
[d] Obtained from Eq. (11) using χ_C determined from heat capacity, using Eq. (10).
[e] Error limits, unless otherwise noted.
[f] Obtained from ΔC_p using Eq. (8).

term. The values of p were found to be positive in some mixtures but negative in others [35–40].

Fig. 2 shows the glass transition temperature vs. aPS content for semicrystalline iPS/aPS blends, crystallized at 190 °C for 12 h (solid circles). Also shown for comparison are the glass transition temperatures of quenched amorphous iPS [15] and blends (open circles). Melt-crystallized samples generally have a slight increase of T_g compared to the quenched amorphous samples. Addition of aPS also systematically drives the glass transition temperature to lower values. T_gs of the semicrystalline iPS/aPS blends can be fitted using Eq. (5) with $k = 0.015$ and $p = -18$. For the quenched amorphous and blends, the fitting parameters k and p are 0.015 and −21, respectively. The large negative value of p indicates a strong intermolecular interaction between aPS and iPS [38–40] regardless of whether the sample is amorphous or crystalline.

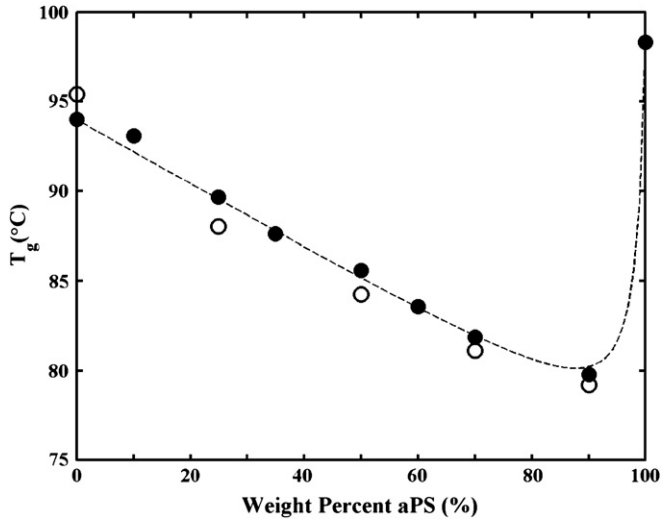

Fig. 2. Glass transition temperature vs. aPS content for iPS/aPS blends. Open circles – wholly amorphous blends; filled circles – blends crystallized at 190 °C for 12 h. Dashed line is the best fit to the semicrystalline blend data using Eq. (5) with $k = 0.015$ and $p = -18$.

The glass transition region was analyzed using the method of Schick and Donth [42] to determine the cooperativity length, ξ_A. According to Schick and coworkers [42,43], the cooperativity length, ξ_A, can be determined from thermal parameters and indicates the level of confinement of amorphous chains. The radius, ξ_A, of cooperative regions of (assumed spherical) volume, V_A, can be found from [42,43]:

$$V_A = k_B T_g^2 \Delta(1/C_V)/(\delta T)^2 \rho = (4\pi/3)\xi_A^3 \quad (6)$$

where k_B is Boltzmann's constant; C_V is the specific heat calculated from C_p at the glass transition by the Nernst equation; and ρ is the sample density. The mean temperature fluctuation, δT, is estimated from the width of the glass transition step (ΔT) as [42,43] $\delta T \sim 0.4\Delta T$. For crystalline iPS/aPS blends, the thermal parameters and calculated cooperativity length, ξ_A, are listed in Table 2.

As aPS content increases from 0% to 50%, the MAF increases while both the crystal fraction and the RAF decrease. However, the crystalline fraction does not have a major influence on the T_g value: from Fig. 2, the quenched amorphous and semicrystalline blend samples have nearly the same T_g at each aPS composition. The major influence is the aPS content, which affects T_g and thus also the cooperativity length in iPS/aPS blends. The value of ξ_A increases steadily with aPS addition. Thus, the large mode lengths of the cooperatively rearranging regions [44] are enhanced by the aPS addition, as indicated by the decrease in T_g, and increase in cooperativity length.

3.2. Thermal analysis of the melting region

Fig. 3a and b shows the normalized heat flow vs. temperature in the vicinity of crystal melting, for different compositions of iPS/aPS blends isothermally melt-crystallized at 190 °C, scanned either at 10 °C/min (Fig. 3a) or at 2 °C/min (Fig. 3b). The curves are presented with the same scaling, but are displaced vertically for clarity. The heat flow has been normalized for total sample mass. The heat flow of

Table 2
Thermal parameters[a] for semicrystalline iPS/aPS blends: transition width, volume and radius of cooperativity region

iPS/aPS	100/0	90/10	75/25	65/35	50/50	40/60	30/70	10/90	0/100
ΔT (°C) ±0.1	12.9	9.7	8.4	8.4	8.7	8.8	7.4	6.1	5.0
V_A (10^{-27} cm^3) ±0.05	4.53	8.48	10.63	11.84	11.41	12.64	18.92	29.05	56.01
ξ_A (nm) ±0.02	1.02	1.27	1.37	1.42	1.41	1.45	1.66	1.91	2.83

[a] Crystallized isothermally at 190 °C for 12 h.

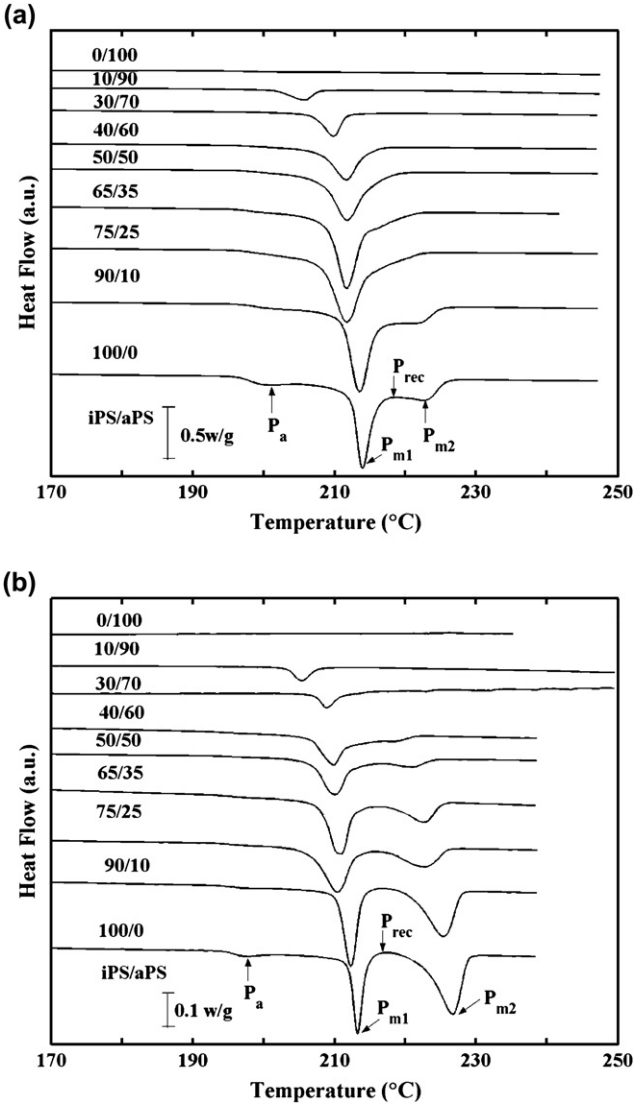

Fig. 3. DSC heat flow vs. temperature for iPS/aPS blends with the indicated compositions melt-crystallized at 190 °C for 12 h. Ordinate values have been normalized for total sample mass, but not for composition of aPS. The curves have been displaced vertically for clarity. Heated at: (a) 10 °C/min; (b) 2 °C/min.

crystallized iPS shows three endothermic peaks labeled P_a (annealing peak), P_{m1} (lower melting peak) and P_{m2} (higher melting peak) in the order of temperature from low to high. Between the two melting peaks, a recrystallization exotherm (P_{rec}) can be observed in some scans (for example, in Fig. 3a and b for pure iPS). With an increase of the aPS component, both P_{rec} and P_{m2} became smaller and eventually disappear.

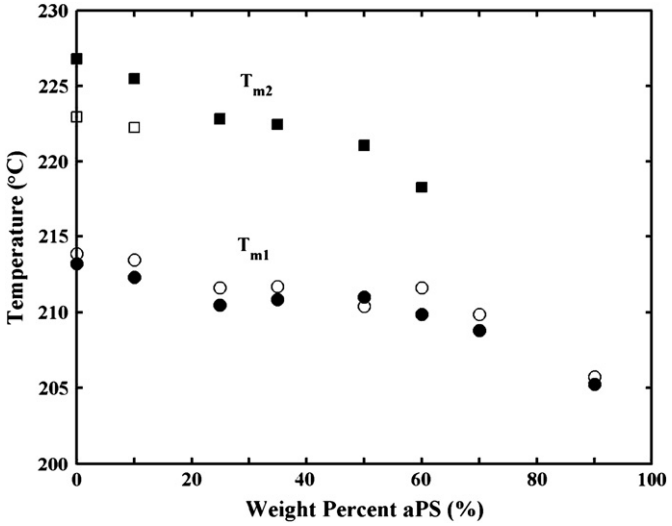

Fig. 4. Melting temperatures of iPS/aPS blends, T_{m1} (circles) and T_{m2} (squares) vs. aPS content, determined from DSC by heating at either 2 °C/min (filled symbols) or 10 °C/min (open symbols).

Fig. 4 shows the melting temperatures vs. aPS content of iPS/aPS blends after DSC scanning with different heating rates. Melting temperature of P_{m1} (T_{m1}) appears over the entire composition range regardless of the heating rate, and decreases with an increase of the aPS component. Melting temperature of P_{m2} (T_{m2}) also decreases with an increase of the aPS component, but disappears when the aPS composition reaches 25% (when heating at 10 °C/min), or 90% (when heating at 2 °C/min).

3.3. Crystalline and rigid amorphous fractions

Semicrystalline iPS has been described with a three-phase model, comprising crystalline, mobile amorphous, and rigid amorphous fractions [14–17]. The degree of crystallinity (χ_C) is obtained from:

$$\chi_C = \Delta H_f(\text{meas})/\Delta H_f \quad (7)$$

where ΔH_f (meas) is the measured heat of fusion from DSC at a heating rate of 10 °C/min, and is determined by integrating the endothermic heat flow from 180 °C to 240 °C.

Since the blends exhibit a single glass transition process, the fraction of the mobile amorphous phase (χ_{MA}) in the semicrystalline iPS/aPS blend can be calculated directly from the ratio of the heat capacity increment of the semicrystalline

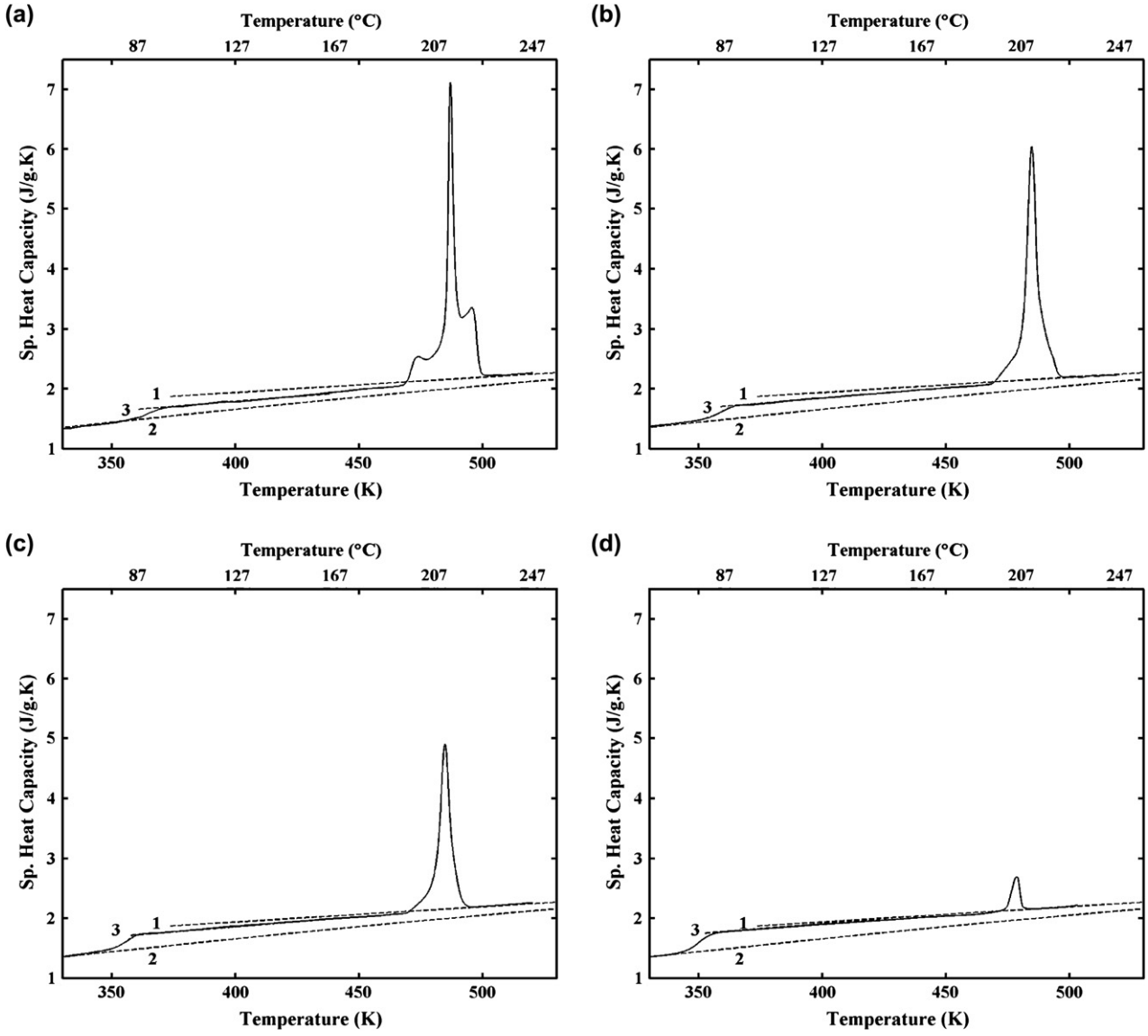

Fig. 5. Specific heat capacity vs. temperature obtained from standard DSC of iPS/aPS blends: (a) 100/0, (b) 75/25, (c) 50/50 and (d) 10/90 – solid curve. Line 1 (dashed) is the heat capacity C_p^{liquid} of 100% liquid, while line 2 (dashed) is the heat capacity of 100% solid, using the data taken from the ATHAS data bank [47]. C_p^{calc}, line 3 (dashed) is determined from Eq. (9) for the blends.

sample, ΔC_p^{sc}, to that of the wholly amorphous sample, ΔC_{p0}, at the glass transition, using [45,46]:

$$\chi_{MA} = \Delta C_p^{sc} / \Delta C_{p0} \tag{8}$$

iPS and aPS have the same heat capacity for 100% solid, C_p^{solid}, and 100% liquid, C_p^{liquid}. In addition, for both aPS and iPS, the measured heat capacity increment of the amorphous material at T_g is $\Delta C_{p0} = 0.3378$ J/g K [15], which is very close to the data from the ATHAS data bank which gives $\Delta C_{p0} = 0.3386$ J/g K [47].

Fig. 5a–d shows the specific heat capacity of pure iPS and several blends. The dotted lines represent the values of C_p^{solid} and C_p^{liquid}, taken from the ATHAS data bank [47], which agree well with the measured data for the heat capacity below T_g, and above the melting point, respectively. The dashed lines labeled (3) represent the calculated heat capacity, C_p^{calc}, for these two samples, under the assumption that all the MAF has relaxed to the mobile liquid state, and only the crystals and RAF remain in the solid state (i.e., $\chi^{solid} = \chi_c + \chi_{RA} = 1 - \chi_{MA}$). The calculation uses:

$$C_p^{calc}(T) = \chi^{solid} C_p^{solid}(T) + \chi_{MA} C_p^{liquid}(T) \tag{9}$$

χ_C and χ_{RA} data from Table 1 were used in the calculation and from Fig. 5 we see that there is a good agreement between the calculated line and the measured data curve above the glass transition heat capacity step, and the slope of the calculated heat capacity (i.e., slope of line 3) lies between the slopes of the (dotted) lines for $C_p^{solid}(T)$ and $C_p^{liquid}(T)$.

Euler's equation was used to calculate the change of crystallinity with temperature using [14,48,49]:

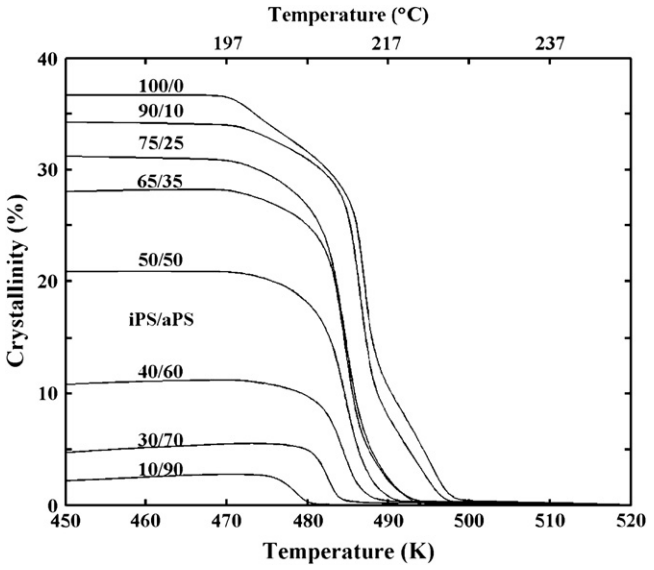

Fig. 6. Weight percent crystallinity, calculated from Eq. (10), vs. temperature for iPS/aPS blends crystallized at 190 °C for 12 h, with the indicated compositions. Blends are heated at 10 °C/min.

$$C_p^{exp}(T) = \chi^{solid} C_p^{solid}(T) + \left(1 - \chi^{solid}\right) C_p^{liquid}(T) - (d\chi_C/dT)\Delta H_f(T) \quad (10)$$

where $C_p^{exp}(T)$ is the experimentally measured specific heat capacity, χ_C is the temperature-dependent crystallinity and $\Delta H_f(T)$ is the temperature-dependent heat of fusion corrected for undercooling by the factor $f = 2T/(T + T_m^\infty)$ [14,48,49] using 242 °C as the infinite crystal melting point, T_m^∞ [14,48,49]. The results are presented in Fig. 6 for the blends. There is no apparent change in χ_C before melting for the blends with weight percent of aPS less than 70%. For the blends with larger weight percent of aPS, such as 70% and 90% (see bottom two curves in Fig. 6), χ_C increases slowly during the heating before melting. The temperature at which χ_C becomes zero decreases as the aPS composition increases.

The fraction of the rigid amorphous phase, χ_{RA}, is calculated in the normal way from a three-phase assumption using:

$$\chi_{RA} = 1 - \chi_{MA} - \chi_C \quad (11)$$

The rigid amorphous fractions are listed in Table 1. Fig. 7 shows χ_{RA} and the ratio χ_{RA}/χ_C vs. aPS content. On the assumption that the RAF constitutes an interfacial layer next to the crystal lamellar surfaces, then the ratio χ_{RA}/χ_C refers to the RAF content in relation to the crystal content. As aPS increases, from homopolymer iPS up to and including the iPS/aPS 50/50 blend, there is no change in the ratio χ_{RA}/χ_C. Over this composition range, the iPS crystallinity has decreased from 0.37 to 0.21 (see Table 1). The rigid amorphous fraction keeps pace with the crystallinity changes, until the aPS content increases beyond 50% at which point χ_{RA}/χ_C increases sharply. In homopolymer PET [18], Androsch and Wunderlich suggested that improvement in the crystal perfection could cause χ_{RA}/χ_C to decrease, as a result of decrease

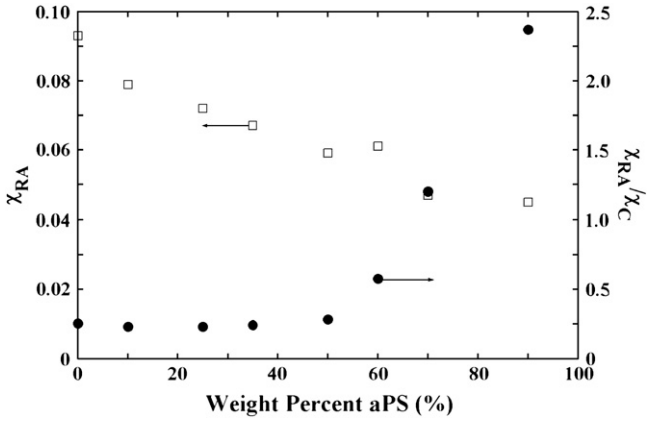

Fig. 7. Phase fractions for crystallized iPS/aPS blends vs. aPS content. Rigid amorphous fraction, χ_{RA} (squares) and ratio of the rigid amorphous fraction to the crystalline fraction, χ_{RA}/χ_C (circles).

in the strain transmitted to the amorphous phase. Here, the increase in χ_{RA}/χ_C may be related to a *decrease* of crystal perfection, and *increase* in the amount of strain between the lamella and the amorphous phase at high content of aPS.

Summarizing the results of thermal analysis, the crystal and rigid amorphous fractions both decrease, while the mobile amorphous fraction increases, as aPS content increases. Addition of aPS causes the glass transition temperature to be depressed. The role of crystals in confining the amorphous phase (causing T_g to shift up in temperature, as observed in iPS homopolymer) is ameliorated by the strong intermolecular interaction between the aPS and the iPS, which mobilizes the amorphous chains (causing T_g to shift down in temperature). The cooperativity length steadily increases as aPS content increases.

Even small addition of aPS causes the endothermic annealing peak, P_A, to vanish. The annealing peak, which is due to the relaxation of rigid amorphous fraction in parallel with melting of a tiny amount of crystals, is retarded with an increase of the composition of aPS, resulting in the slow devitrification of RAF in parallel with the melting of large amount of crystals. Both of the higher melting peaks, P_{m1} and P_{m2}, move to lower temperature with aPS addition. T_{m2} decreases most likely as a result of inability of the iPS crystals to reorganize during DSC scanning. Furthermore, the uppermost endotherm peak is steadily suppressed by aPS addition (as it is with faster heating rate), consistent with suppression of the ability of the iPS crystals to reorganize or recrystallize during DSC scanning. The inability of iPS crystals in iPS/aPS blends to reorganize in blends with the higher aPS contents may be related to lamellar stack morphology, i.e., a reduced amount of mobile amorphous phase located between the lamellar stacks, a suggestion that will be examined in the next section.

3.4. X-ray scattering studies

Wide angle X-ray scattering intensity is shown in Fig. 8a for iPS/aPS blends crystallized at 190 °C for 12 h. Miller indices are shown above the major reflections. The (211) peak decreases as the content of aPS increases, as shown by the arrow

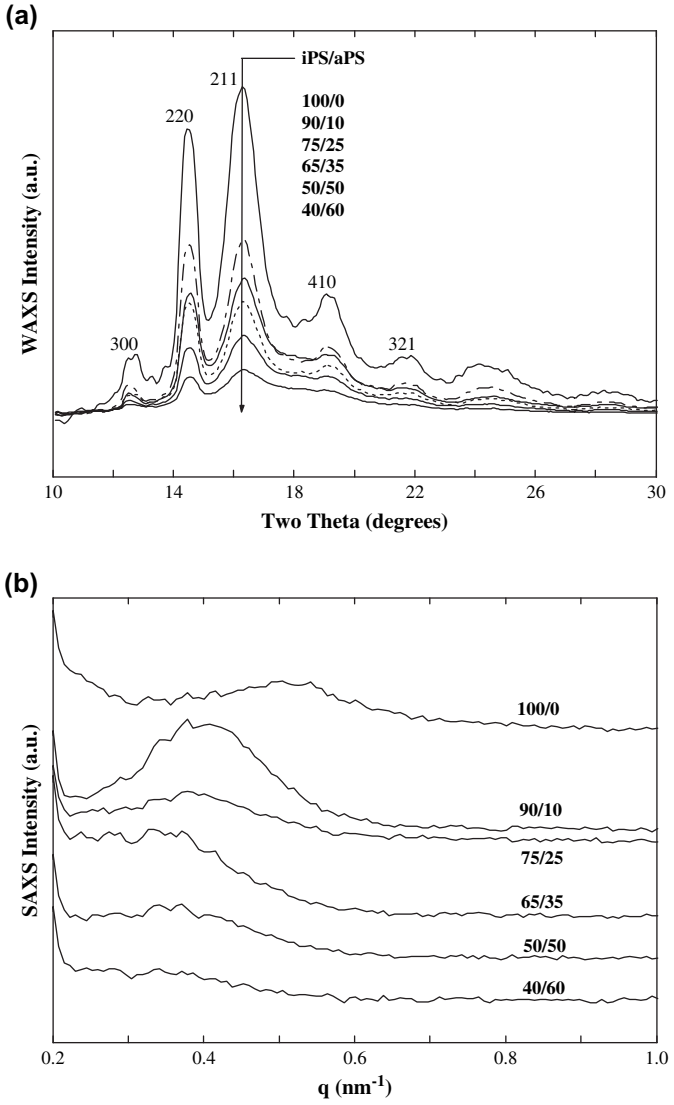

Fig. 8. X-ray scattering results ($\lambda = 0.371$ nm) for iPS/aPS blends at the compositions indicated. (a) WAXS intensity vs. scattering angle, 2θ. Miller indices are shown above the major reflections. (b) SAXS intensity vs. q-vector.

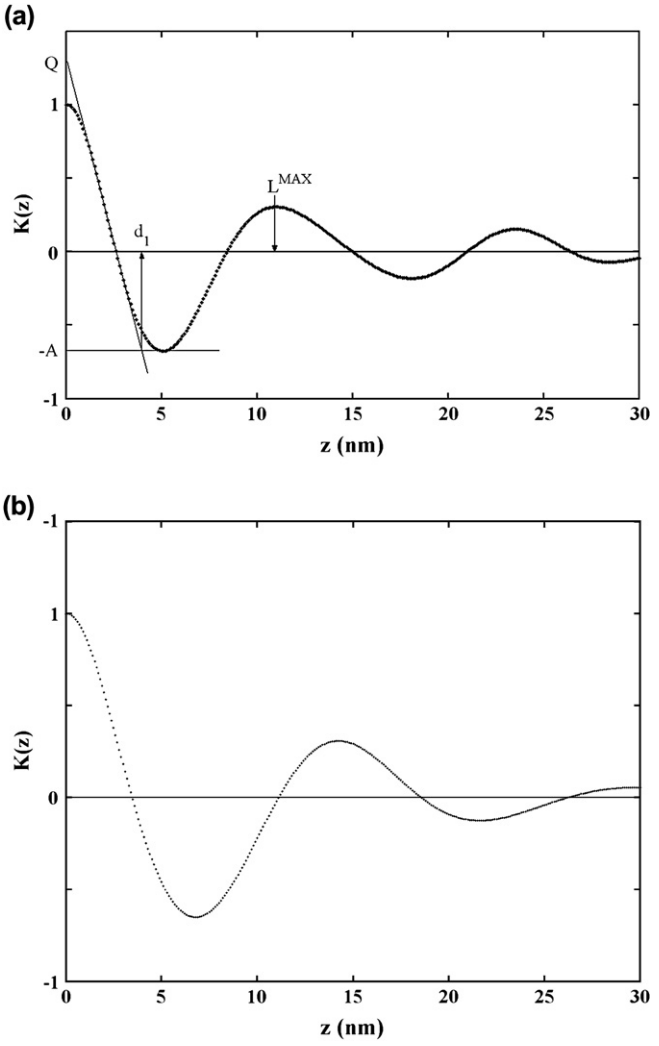

Fig. 9. One-dimensional electron density correlation function, $K(z)$, vs. z, the dimension perpendicular to the lamellar stacks, for iPS/aPS blends: (a) 100/0 and (b) 75/25. In part (a), the first maximum past $z = 0$ indicates the long period, L^{MAX}. The thickness of phase 1, d_1, is found from the z-coordinate of the intersection of the linear fit of the data at low z, with the baseline at $-A$, according to the method of Strobl and Schneider [34]. The self-correlation triangle has sides d_1 and $|-A| + Q$.

in the figure. The WAXS peaks become less distinct, and the degree of crystallinity, judged qualitatively from the relative area of the crystal reflections to the total coherent scattering, decreases with an increase in aPS content. SAXS data for blends with different aPS content are shown in Fig. 8b.

Observation of the Bragg peak indicates that the iPS/aPS blends can be considered to comprise two-dimensional lamellar stacks, with alternating crystal and amorphous regions as has been done for iPS [50,51]. The Bragg scattering peak in the $I(q)$ vs. q plots is weak, because of the close values of amorphous and crystalline bulk density, which results in weak scattering contrast from the lamellar stacks. No SAXS scattering peak could be detected in blends with aPS content greater than 60%. In spite of weak SAXS peaks in I vs. q plots, the Lorentz-corrected intensity shows a clear peak but is omitted for the sake of brevity.

The Lorentz-corrected intensity, $I(q)q^2$ vs. q, was used to determine the one-dimensional electron density correlation function according to Eq. (4), from which the lamellar stack parameters were obtained. Typical results for $K(z)$ are shown in Fig. 9a and b for iPS/aPS 100/0 and 75/25, respectively. Using the method of Strobl and Schneider [34], the first maximum past $z = 0$ is the lamellar stack periodicity, L^{MAX}. The thickness of one phase, d_1, is found as shown in Fig. 9a, from the self-correlation triangle. Table 3 lists SAXS parameters of iPS/aPS blends. Included in the table are the volume fractions of phase 1, V_1, determined from either d_1/L^{MAX} or from the self-correlation triangle using $|-A|/(|-A| + Q)$ [34]. For comparison, the volume fraction crystallinity, ϕ_1, from heat capacity analysis is also listed in Table 3.

The lamellar stack parameters are plotted in Fig. 10a and b. Bragg long period, L_B, from the maximum of $I(q)q^2$ vs. q is compared to L^{MAX} in Fig. 10a. L_B (open squares) is nearly always greater than L^{MAX} (filled circles), which is typical. One

Table 3
Structural parameters of semicrystalline iPS/aPS blends

	iPS/aPS					
	100/0	90/10	75/25	65/35	50/50	40/60
L_B[a] (nm, ±0.2)	11.7	14.5	15.3	16.6	15.1	15.6
L^{MAX}[b] (nm, ±0.2)	11.0	14.1	14.2	15.4	14.8	15.9
d_1[c] (nm, ±0.2)	4.1	5.0	5.3	5.2	4.1	4.7
V_1[d] (%, ±2)	37	35	37	34	28	29
V_1[e] (%, ±2)	35	34	34	33	28	29
ϕ_1[f] (%, ±1)	35	33	30	27	20	11
L_R (nm, ±0.2)	1.1	1.3	1.3	1.3	1.3	2.6
L_{Mi} (nm, ±0.2)	6.5	8.2	8.7	10.1	8.7	7.3
ϕ_{Mi} (%, ±2)	56	55	49	52	42	17
ϕ_{Mo} (%, ±2)	0	0	14	15	32	66

[a] Long period determined from the peak in $I(q)q^2$ vs. q.
[b] Long period determined from the first maximum past $z = 0$ in $K(z)$.
[c] Phase 1 thickness determined from the self-correlation triangle (see Fig. 9a).
[d] Volume fraction of phase 1, from d_1/L^{MAX}, expressed as a percent.
[e] Volume fraction of phase 1, from $|-A|/(|-A| + Q)$, expressed as a percent.
[f] Volume fraction crystallinity from heat capacity analysis, using Eq. (1).

exception (for 60% aPS) is within the error bars on the measurement. From this plot we conclude that the lamellar stack period is greater in all the blends compared to homopolymer iPS. As the aPS content increases, there is a slight trend for the lamellar stack period to increase.

Fig. 10b compares the volume fraction crystallinity ϕ_1 (filled squares) and V_1 from d_1/L^{MAX} (open circles). ϕ_1, determined from heat capacity measurements, decreases steadily as aPS content increases. V_1 and ϕ_1 are very close in iPS homopolymer and 90/10 iPS/aPS blend and V_1 is much greater than ϕ_1 in the blends with aPS content higher than 25%. From Babinet's principle of reciprocity, the thickness of phase 1 from SAXS cannot be assigned unambiguously either to the crystalline or to the amorphous layer. But V_1 could be assigned to crystalline volume fraction and V_2 to amorphous volume fraction within the lamellar stacks with the help of DSC results. To determine the morphology and the location of amorphous fraction of the blends, we treat each blend individually by comparing the linear crystallinity V_1 from SAXS with the crystallinity ϕ_1 from DSC. Thus, in iPS homopolymer and in the 90/10 blend, V_1 and ϕ_1 are very close, suggesting that the amorphous fraction is located inside the lamellar stacks. V_1 is much greater than ϕ_1 in the blends with aPS content greater than 25%. The departure of V_1 from ϕ_1 suggests that a part of the amorphous phase is outside the lamellar stacks in interfibrillar or interspherulitic regions.

For a two-component polymer blend, there are three locations for the mobile amorphous fractions, commonly known as interlamellar region (between lamellae), interfibrillar region (between lamellar bundles), and interspherulitic region (between spherulites). Warner and coworkers [4] studied mixtures of iPS with aPS, where the content of aPS ranged from 0% to 30%. Using SAXS they found no apparent change in Bragg long period with an increase of aPS, and concluded that aPS was trapped in the interfibrillar region of the iPS spherulites, and additionally, the melting temperature was constant for all the blends they studied. The miscibility of their blends

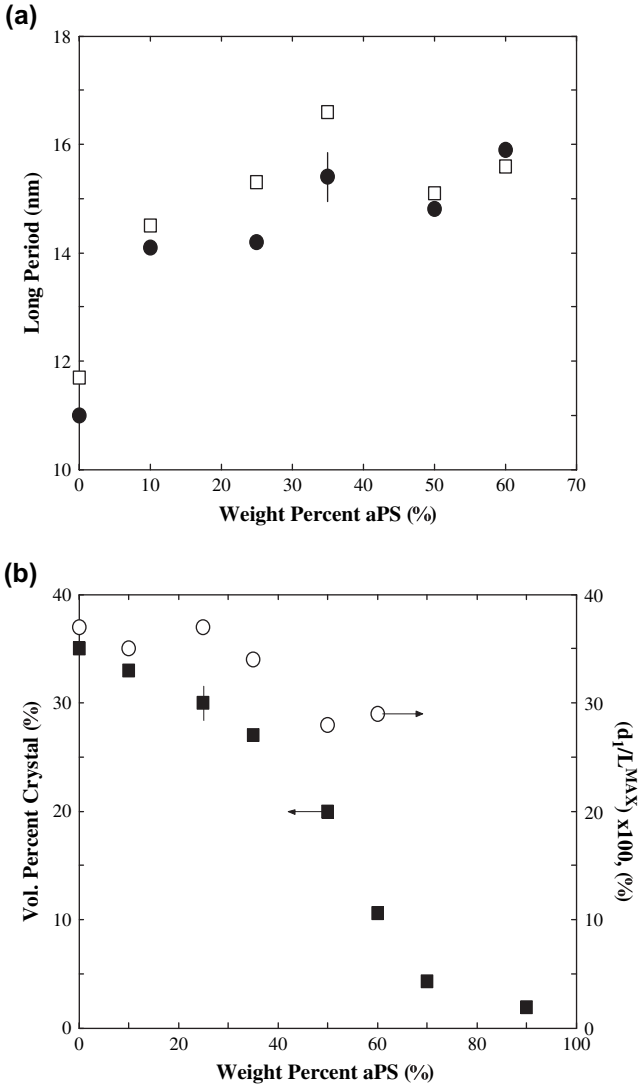

Fig. 10. Small angle X-ray scattering parameters vs. aPS content, in semicrystalline iPS/aPS blends. (a) Long period. L_B (open squares) from the maximum in the Lorentz-corrected intensity; L^{MAX} (filled circles) from the first maximum past $z = 0$ in the correlation function. (b) Crystalline volume fraction (filled squares) from Eq. (1); volume fraction of phase 1, $V_1 = d_1/L^{MAX}$, is determined from the self-correlation triangle, using the method of Strobl and Schneider [34]. Representative error bars are indicated, and apply to all data points.

was not reported. Wang and coworkers [1] studied sPS/aPS blends using TEM, and concluded that added aPS molecules are rejected outside the sPS lamellar stacks, located within interfibrillar or interspherulitic regions.

Our miscible blends of iPS and aPS are different from Warner's: both lamellar thickness and Bragg long period change with an increase of aPS. And, although the lamellar thickness increases, the melting temperature decreases slightly (see Fig. 4). Yeh and Lambert [7] suggested that the melting temperature for iPS/aPS blends is depressed with aPS molecular weight below 51,000 g/mol but was constant above 51,000 g/mol. So the difference between Warner's results and ours is likely to be due to the different molecular weights of aPS (270,000 g/mol for Warner and 45,000 g/mol for our

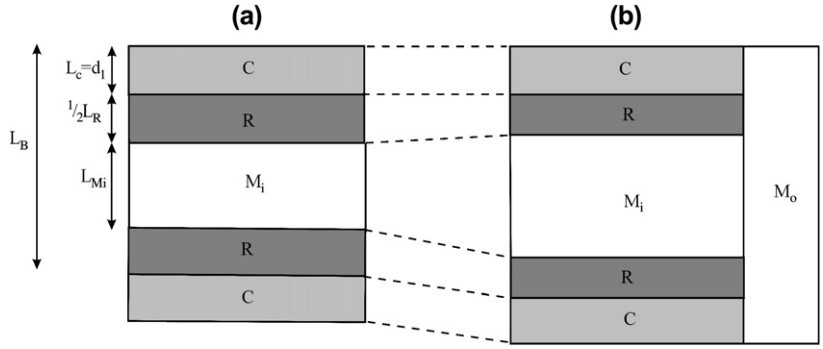

Fig. 11. Schematic representations of the structural models for representative semicrystalline iPS/aPS blends: (a) aPS < 25%; (b) aPS > 25%. Crystal lamella (C – light grey), rigid amorphous layer (R – dark grey), mobile amorphous layer inside or outside the lamellar stacks (Mo, Mi – white). L_C, L_{Mi}, L_R are the thicknesses of the crystal lamella, mobile amorphous layer inside the lamellar stacks, and rigid amorphous layers, respectively. The Bragg long period, L_B, comprises one lamellar crystal and the intervening amorphous phase. The dashed lines indicate that the lamellar thickness remains about the same, rigid amorphous layer thickness decreases, and the Bragg long period increases as a function of aPS content.

work). Different molecular weights can result in the different locations of aPS, causing the aPS component to affect the iPS lamellae differently.

The scheme of the lamellar structures is presented in Fig. 11a and b for two different aPS ranges, aPS $\leq$ 25% and aPS > 25%, respectively. The phase structure shows crystalline lamellae, C, mobile amorphous, M, and rigid amorphous, R, fractions and their organization. The mobile amorphous fraction inside (Mi) or outside (Mo) the stacks is indicated. As shown in the figure, the long period, L_B, comprises the crystal thickness, L_C, two rigid amorphous layer thicknesses, L_R, and the thickness of the mobile amorphous fraction within the stack, L_{Mi}. The corresponding volume fractions of the amorphous phase inside or outside the stack are designated as ϕ_{Mi} or ϕ_{Mo}. On the assumption that the crystal thickness can be associated with the thickness of phase 1 from the correlation function analysis, then the quantities L_R, L_{Mi}, ϕ_{Mi} and ϕ_{Mo} can be directly obtained by using:

$$L_R = \phi_R L_C/\phi_1 = (1-\phi_1)[\chi_R(1-\chi_C)]d_1/\phi_1 \quad (12)$$

$$L_{Mi} = L_B - d_1 - L_R \quad (13)$$

$$\phi_{Mi} = L_{Mi}\phi_1/d_1 \quad (14)$$

$$\begin{aligned}\phi_{Mo} &= 1-\phi_1-\phi_R-\phi_{Mi} \\ &= 1-\phi_1-(1-\phi_C)[\chi_R/(1-\chi_C)]-\phi_{Mi}\end{aligned} \quad (15)$$

where ϕ_R is the volume fraction of the rigid amorphous phase. The results of these calculations are shown in Table 3. Values of L_R, while small, are quite similar to what we observed before in homopolymer iPS [50]. With an increase of aPS content, more amorphous phase is rejected outside the lamellar stacks, a result that is similar to what was observed in sPS/aPS blends [1]. Comparing the results of Tables 2 and 3, we see that L_R is always less than $2\xi_A$ while L_{Mi} is always larger than $2\xi_A$, a result similar to what we observed with iPS homopolymer [50]. The $L_{Mi} > 2\xi_A$ suggests that the amorphous phase within the lamellar stacks is large enough to undergo the cooperative segmental motions needed for expression of the long mode lengths of the glass transition. Thus, it is likely that in blends with the larger aPS contents, the interlamellar (Mi) and extra-lamellar (Mo) amorphous chains (including both interfibrillar and interspherulitic amorphous chains) both can contribute to the glass transition.

As is known generally, observation of a single T_g suggests full miscibility within a region of the order 20–40 nm, but it does not imply full miscibility on a smaller, more localized size scale [52,53] where heterogeneity may exist. For example, the blend system poly(vinyl phenol)/poly(methyl methacrylate), PVPh/PMMA, has been observed to exhibit only a single T_g based on DSC studies [54]. However, two relaxations related with the glass transition were found by using dynamic mechanical analysis [55], and these were suggested to arise from micro-heterogeneous regions, i.e., to different local organizations, even though the blends were miscible [53]. This phenomenon also has been found in other polymer blends such as poly(ε-caprolactone)/chlorinated polyethylene, PCL/PECl [52], and poly(vinyl chloride)/PCL, PVC/PCL [53]. In our case, the iPS/aPS blends are also fully miscible based on the single T_g, but possess different microstructures, including different degrees of crystallinity, different RAF fractions, different locations of the mobile amorphous fraction, and different cooperativity lengths.

4. Conclusions

1. Thermal analysis shows that the crystal and rigid amorphous fractions both decrease, while the mobile amorphous fraction increases, as aPS content increases.
2. Addition of aPS causes the glass transition temperature to be depressed. The role of crystals in confining the amorphous phase (causing T_g to shift up in temperature) is ameliorated by the strong intermolecular interaction of the aPS which mobilizes the amorphous chains (causing T_g to shift down in temperature).
3. Even small addition of aPS causes the endothermic annealing peak, P_A, to vanish. Both of the higher melting peaks P_{m1} and P_{m2} move to lower temperature with aPS

addition. At high aPS content, above 50%, aPS addition results in the formation of less perfect crystals that melt at lower temperatures, a result confirmed by WAXS.

4. Furthermore, the uppermost endotherm peak of iPS is steadily suppressed by aPS addition (as it is with faster heating rate [17]), consistent with suppression of the ability of the iPS crystals to reorganize or recrystallize during DSC scanning. The inability of iPS crystals to reorganize may be related to a decrease of crystal perfection, and increase in the amount of strain between the lamella and the amorphous phase at high content of aPS.

To explain the slight decrease in measured melting temperature, T_m, we look at the Gibbs–Thomson equation [56],

$$T_m = T_m^\infty - 2\sigma T_m^\infty / (\Delta h_m n^*) \quad (16)$$

where T_m^∞ is the equilibrium melting temperature, σ is the fold surface free energy per monomer at the basal crystallite surfaces, Δh_m is the heat of fusion per monomer, and n^* is the lamellar thickness. An increase of n^* (as observed in Table 3) but a decrease of T_m with addition of aPS might be interpreted either by an increase of σ, or by a decrease in T_m^∞. Reduction of the T_m^∞ has been measured in other binary blends [12]. Further work will be necessary to determine which effect is operational in the present case.

5. X-ray scattering shows that the long period in the iPS/aPS blends is greater than in the iPS homopolymer, and long period increases slightly as aPS content increases. Comparison of the volume fraction of phase 1 with the volume fraction crystallinity from DSC suggests that more and more amorphous phase is rejected outside the lamellar stacks as aPS content increases.
6. The effect of aPS addition is to reduce the confinement of the amorphous phase chains. The cooperativity length, ξ_A, which is calculated from thermal analysis of the glass transition, increases with aPS addition. The interlamellar and extra-lamellar amorphous chains both contribute to the glass transition relaxation process, therefore, the cooperativity length cannot be assigned to a specific location, either intra-lamellar or extra-lamellar.

Acknowledgements

The authors thank the National Science Foundation for support of this work through the Polymers Program of the Division of Materials Research under DMR-0602473 and the MRI Program under DMR-0520655 for thermal analysis instrumentation.

References

[1] Wang C, Lin CC, Tseng LC. Polymer 2006;47:390.
[2] Wang C, Liao WP, Cheng YW. Polymer 2004;45:961.
[3] Wang C, Liao WP, Wang ML. Polymer 2004;45:973.
[4] Warner FP, MacKnight WJ, Stein RS. J Polym Sci Polym Phys Ed 1977;42:777.
[5] Okada T, Saito H, Inoue T. Polymer 1994;35:5699.
[6] Boon J, Azcue JM. J Polym Sci A2 1968;6:885.
[7] Yeh GS, Lambert SL. J Polym Sci A2 1972;10:1183.
[8] Keith HD, Padden FJ. J Appl Phys 1964;35:1270.
[9] Keith HD, Padden FJ. J Appl Phys 1964;35:1286.
[10] Cebe P, Chung SY. J Mater Sci 1990;25:2367.
[11] Huo PP, Cebe P. Macromolecules 1993;26:5561.
[12] Huo PP, Cebe P. Macromolecules 1993;26:4275.
[13] Huo PP, Cebe P. Macromolecules 1993;26:3127.
[14] Xu H, Cebe P. Macromolecules 2004;37:2797.
[15] Xu H, Ince BS, Cebe P. J Polym Sci Polym Phys Ed 2004;41:3026.
[16] Xu H, Cebe P. Polymer 2006;46:8734.
[17] Minakov A, Mordvintsev D, Tol R, Schick C. Thermochim Acta 2006;442:25.
[18] Androsch R, Wunderlich B. Polymer 2005;46:12556.
[19] Huo PP, Cebe P. Macromolecules 1992;25:902.
[20] Lu X, Cebe P. Polymer 1996;37:4857.
[21] Boon J, Challa G, Van Krevelen D. J Polym Sci Part A Gen Pap 1968;2:1791.
[22] Lemstra PJ, Kooistra T, Challa G. J Polym Sci Polym Phys Ed 1974;12:1565.
[23] Plans J, MacKnight WJ, Karasz FE. Macromolecules 1984;17:810.
[24] Petrillo E, Russo R, D'Aniello C, Vittoria V. J Macromol Sci Phys 1998;37:15.
[25] Blundell DJ. Polymer 1987;28:2248.
[26] Liu T, Petermann J. Polymer 2001;42:6453.
[27] Chung JS, Cebe P. Polymer 1992;33:2312.
[28] Petermann J, Gohil RM. J Macromol Sci Phys 1979;B16(2):177.
[29] Pyda M, Wunderlich B. Macromolecules 2005;38:10472.
[30] Brandup J, Immergut EH. Polymer handbook. New York: Wiley Interscience; 1989. p. V81–5.
[31] Ruland W. Colloid Polym Sci 1977;29:255.
[32] Koberstein JT, Morra B, Stein RS. J Appl Crystallogr 1980;34:23.
[33] Vonk C, Kortleve G. Kolloid Z Z Polym 1967;19:220.
[34] Strobl G, Schneider MJ. J Polym Sci Part B Polym Phys 1980;18:143.
[35] Fox TG. Bull Am Phys Soc 1956;1:123.
[36] Gordon M, Taylor JS. J Appl Chem 1952;2:496.
[37] Tsutsui T, Nakano H, Tanaka R, Tanaka T. Kobunshi Ronbunshu 1978;35:517.
[38] Kwei TK. Macromolecules 1987;20:174.
[39] Pennacchia J, Pearce E, Kwei TK. Macromolecules 1986;19:973.
[40] Zheng S, Mi Y. Polymer 2003;44:1067.
[41] Meaurio E, Zuza Ester, Sarasua JR. Macromolecules 2005;38:1207.
[42] Schick C, Donth E. Phys Scr 1991;43:423.
[43] Dobbertin J, Hensel A, Schick C. J Therm Anal 1996;47:1027.
[44] Adam G, Gibbs JH. J Chem Phys 1965;43:139.
[45] Cheng SZD, Cao MY, Wunderlich B. Macromolecules 1986;19:1868.
[46] Cheng SZD, Wu ZQ, Wunderlich B. Macromolecules 1987;20:2802.
[47] Pyda M, editor. ATHAS data bank, <http://athas.prz.edu.pl/databank/welcome-db.html>; 1997.
[48] Pyda M, Di Lorenzo M, Park J, Kamasa P, Wunderlich B. J Polym Sci Part B Polym Phys 2001;39:1594.
[49] Di Lorenzo M, Pyda M, Wunderlich B. J Polym Sci Part B Polym Phys 2001;39:1549.
[50] Natesan B, Xu H, Ince BS, Cebe P. J Polym Sci Polym Phys Ed 2004;42:777.
[51] Miyamoto Y, Fukao K, Miyaji H. Colloid Polym Sci 1995;273:66.
[52] Plivelic TS, Silvana NC, Goncalves MDC, Torriani IL. Macromolecules 2007;40:253.
[53] Kuo SW, Chan SC, Chang FC. Macromolecules 2003;36:6653.
[54] Serman CJ, Painter PC, Coleman MM. Polymer 1991;32:1049.
[55] Li D, Brisson J. Macromolecules 1996;29:868.
[56] Strobl G. The physics of polymers. New York: Springer Press; 1997.